Electronic supplementary information for

Removal of Residual Contaminants by Minute-level Washing Facilitates the Direct Regeneration of Spent cathodes from Retired EV Li-ion Batteries

Yi Guo,[ah] Yang Li,[bcdh] Kai Qiu,[d] Yan Li,[e] Weijing Yuan[b], Chenxi Li,[b] Xinyu Rui,[a] Lewei Shi,[b] Yukun Hou,[a] Saiyue Liu,[a] Dongsheng Ren,[a]* Tiening Tan,[d]* Gaolong Zhu,[d] Languang Lu,[a] Shengming Xu,[f] Biao Deng[g], Xiang Liu,[b]* and Minggao Ouyang[a]*

[a.] School of Vehicle and Mobility, Tsinghua University, Beijing 100084, P. R. China
[b.] School of Material Science and Engineering, Beihang University, Beijing 100191, P. R. China
[c.] School of Transportation Science and Engineering, Beihang University, Beijing, 100191, P. R. China
[d.] Prof. Ouyang Minggao Academician Workstation, Sichuan New Energy Vehicle Innovation Center Co., Ltd., Sichuan, 644000, P. R. China
[e.] Beijing Key Laboratory of Microstructure and Properties of Solids, Faculty of Materials and Manufacturing, Beijing University of Technology, Beijing 100124, P. R. China
[f.] Institute of Nuclear and New Energy Technology, Tsinghua University, Beijing 100084, P. R. China
[g.] Shanghai Institute of Applied Physics, Chinese Academy of Sciences, Shanghai 201204, P. R. China
[h.] These authors contributed equally

*Correspondence: rends@tsinghua.edu.cn, tiening.tan@sevc.com.cn, xiangliu@buaa.edu.cn, ouymg@tsinghua.edu.cn

1. Materials and Methods

Collecting and cleaning degraded cathode materials: Retired electric vehicle battery modules were automatically disassembled after discharge, sorted, and separated into individual components such as electrodes, metal casing, and separators. Cathode electrodes were dried and then calcined in a muffle furnace at 400°C to remove the organic solvent and partly decompose the polyvinylidene fluoride (PVDF) binder. Subsequently, the separated cathodes electrodes were crushed, and most of aluminum current collectors and other impurities were removed from obtained black mass through a combination of manual-assisted work, crushing, sieving, magnetic separation, and so on. Based on the metal residual analysis (**Table S3**), the collected black mass, mainly consisting of spent cathode material, was used for regeneration.

To remove residual impurities, the spent cathodes underwent a 5-minute ultrasonic washing in the HNO_3 diluent, with a mass ratio of spent cathodes to cleaning solution of 1: 10. After the first centrifugation, the cathode material was rinsed with deionized (DI) water, and then the newly formed suspension was centrifuged three times. Finally, the cleaned powder was dried at 60°C for 12 hours under a vacuum and subsequently used for the regeneration and characterization. All processes are illustrated in **Fig. S1**.

Regeneration of degraded cathode material: The degraded cathode material was regenerated through solid sintering to obtain regenerated material. Before regeneration, the cleaned NCM cathode material from spent LIBs (C-NCM) was mixed with lithium carbonate (Li_2CO_3, 98%, Aladdin), with a lithium-to-transition metal molar ratio (Li/TM) of 1.08 according to the inductively coupled plasma optical emission spectrometry (ICP-OES) results of C-NCMs. The powder mixture was calcined at 850°C for 10 hours in an oxygen atmosphere, with a heating rate of 10°C min^{-1}, and then cooled down naturally. Spent NCM cathode material without cleaning (S-NCM) was regenerated in the same process. The regenerated NCM cathode material (R-C-NCM and R-S-NCM) was ground into a uniform powder for coin half-cell assembly and other characterization.

Coin cell assembly and electrochemical performance: To evaluate the electrochemical performance of the cathode material, the coin cell was assembled. The cathode materials were mixed with conductive carbon (Super P) and PVDF in 1-methyl-2-pyrrolidone (NMP) using a Thinky mixer (ARE-310, Thinky Co., Japan). The mass ratios of cathode materials to Super P to PVDF were 8∶1∶1. The obtained slurry was stirred for 2 hours and then cast on an aluminum foil using a film applicator, maintaining areal mass loading of active material 3.6 mg cm^{-2}, followed by overnight drying at 120°C in a vacuum oven. The electrodes were cut into round pieces before coin cell assembly. Coin cells were assembled using Li metal foil (4 mm thick) as the anode, a polyethylene separator (Celgard 2320), 1 M $LiPF_6$ electrolyte dissolved in a solvent mixture (ethylene carbonate (EC) : dimethyl carbonate (DMC) : ethyl methyl carbonate (EMC) in a volume ratio of 1:1:1) as the electrolyte (80 μL) in a glove box filled with pure argon (O_2 and H_2O partial pressure < 0.1 ppm). The cells were allowed to rest for at least 6 hours before testing. The calendaring pressure is 800 MPa for assembling the coin cell.

All coin cells were tested at room temperature using the battery tester (CT2001A, Wuhan Land Electronic Co. Ltd., China). In the long-term cycling, the coin cell was cycled at 0.1 C for three cycles before cycling at 0.3 C (1 C = 150 mAh g^{-1}) between 2.8–4.4 V (vs. Li/Li^+). In the rate

capability test, the coin cell was first tested at 0.1 C for three cycles and then at 0.2, 0.5, 1, 2, and 3 C each for five cycles, within the aforementioned potential range. Electrochemical impedance spectroscopy (EIS) measurement was performed in a frequency range from 100 kHz to 0.01 Hz with a potential amplitude of 5 mV to compare Li^+ transport in different samples. Cyclic voltammetry (CV) measurements were carried out using the Multi Autolab (M204, Metrohm) with a voltage range of 2.8–4.4 V at different scan rates. The slope of fitting line about the square root of scan rates ($v^{1/2}$) versus the peak current (I_p) stands for Li diffusion speed based on the Randles–Sevcik equation.[1] The galvanostatic intermittent titration technique (GITT) data was collected using a current pulse of 0.05 C for 30 minutes, with a time interval of 30 minutes. These data are used to quantitatively determine Li-ion diffusion coefficient (D_{Li^+}).[2]

Structural characterization and chemical analysis: Scanning electron microscope (SEM) was carried out to characterize morphology on the Zeiss Crossbeam 540. X-ray diffraction (XRD) was used to determine crystal structure using a Bruker D8 X-ray diffractometer (Cu Ka radiation). For simulating direct heating regeneration, in situ XRD for hearting in the O_2 atmosphere and 1st cycling was performed using an X-ray diffractometer equipped with a hot stage (TS1500, Linkam Scientific Instruments) and a battery tester (Wuhan Land Electronic Co. Ltd., China). The XRD patterns were continuously collected in the temperature range of 30–900 K at a heating rate of 10°C min^{-1}. the software GSAS-II was used for the Rietveld refinement. Following the high angle annular dark field scanning transmission electron microscopy (HAADF-STEM) specimen preparation was conducted using focused ion beam (FIB) cutting on a Zeiss Crossbeam 540, double Cs-Corrected STEM (JEM-ARM300F, Japan) was employed to characterize microscopic phase structure.

The regeneration of NCMs includes cleaning impurities and repairing the structure. SEM combined with time-of-flight secondary ion mass spectrometry (SEM-ToF-SIMS) combined system (ION-TOF GmbH, Germany) was used to detect the distribution of impurities on the cathode particles. X-ray photoelectron spectroscopy (XPS) was performed on a Thermo Scientific Nexsa G2 system to analyze the surface chemical compositions of the cathode material. ICP-OES analysis was carried out on an iCAP 7600 ICP-OES Analyzer from Thermo Fisher Scientific for quantitative element composition determination. The properties of the impurity layer were examined using Fourier-transform infrared (FTIR) spectroscopy (Vertex 70v, Bruker). The analysis of metal scraps in spent cathodes was confirmed using a Thermo Scientific Phenom ParticleX. The heat behavior and gas release of mixer containing spent cathodes and lithium salt were characterized using STA449F5-QMS403D (NETZSCH, Germany). The mass loss of spent cathodes was investigated using TA SDT650 (TA Instruments, USA).

2D TXM–XANES measurements were conducted at the 3D nano image beamline (BL18B) at the Shanghai Synchrotron Radiation Facility (SSRF). For sample preparation, cathode particles were directly loaded into capillaries using a syringe, and the capillaries were then secured on the sample bench. A total of 147 energy points, ranging from 8.18 to 8.56 keV, were used to index the white line peak position and determine the Ni valence state. The TXM–XANES data were processed using TXM-wizard software.

Calculation of the diffusion energy barrier and mean square displacement: To calculate the comparable thermodynamic barrier of Li^+ hopping inside representative residue, density functional theory (DFT) calculation using DMol^3 was carried out and we kept the amount of movable Li^+

number similar in constant space through designing the supercell volume (LiF set to 1×2×2, Li_2CO_3 set to 1×1×1 and LiOH set to 1×2×2) for different crystal structure models. As the exchange-correlation description, the global gradient approximation (GGA) with Perdew Burke Ernzerhof (PBE) was used.[3] Through the complete Linear Synchronous Transit (LST) and the Quadratic Synchronous Transit (QST) methods, the transition state (TS) search jobs with the RMS convergence setting to 0.01 Ha $Å^{-1}$ were used to calculate the migration barrier energy (ΔE_{Li^+}).

For getting the mean square displacement of the Li atom, the applied atom models from the Materials Project were imported. All the structures were optimized using the Dmol[3] module of Materials Studio, GGA-PBE functional[3]. The details are as follows: the SCF tolerance was set to 1E−06 Ha $Å^{-1}$, the core treatment is all-electron, the basis was set to DND, and the K-points of the NCM, LiF, and Li_2CO_3 cells were set to 2×2×1, 3×3×3, and 3×2×1, respectively. These supercells (a 10×10×4 supercell for the NCM cathodes phase, a 7×7×4 supercell for the LiF phase, and a 6×5×1 supercell for the Li_2CO_3 phase) were annealed and the respective amorphous structures of LiF and Li_2CO_3 were obtained using the Forcite module of the software package Materials Studio with the constant-number, -pressure, and -temperature (NPT) ensemble, universal force field[4], the temperature setting to 1000 K, Nose−Hoover thermostat. Finally, the (010) surface of the NCM cathode was used for building the NCM // Li_2CO_3 // Li_2CO_3 and NCM // LiF // Li_2CO_3 model with 7680 atoms and 7808 atoms, respectively, with an initial distance based on 3 Å vacuum spaces. molecular dynamics simulations were performed using the Materials Studio Forcite. The simulations were carried out with the constant-number, -volume, and -temperature (NVT) ensemble and universal forcefield. And the temperature was set at 298 K with a Nose−Hoover thermostat. the integration time step was 1 fs during the total time of 20 ns. Then, the MSD curve of the Li atoms was obtained to analyze the diffusivity ($Diff_{Li^+}$) of Li-ion in two models.

2. Supplementary Figures and Tables

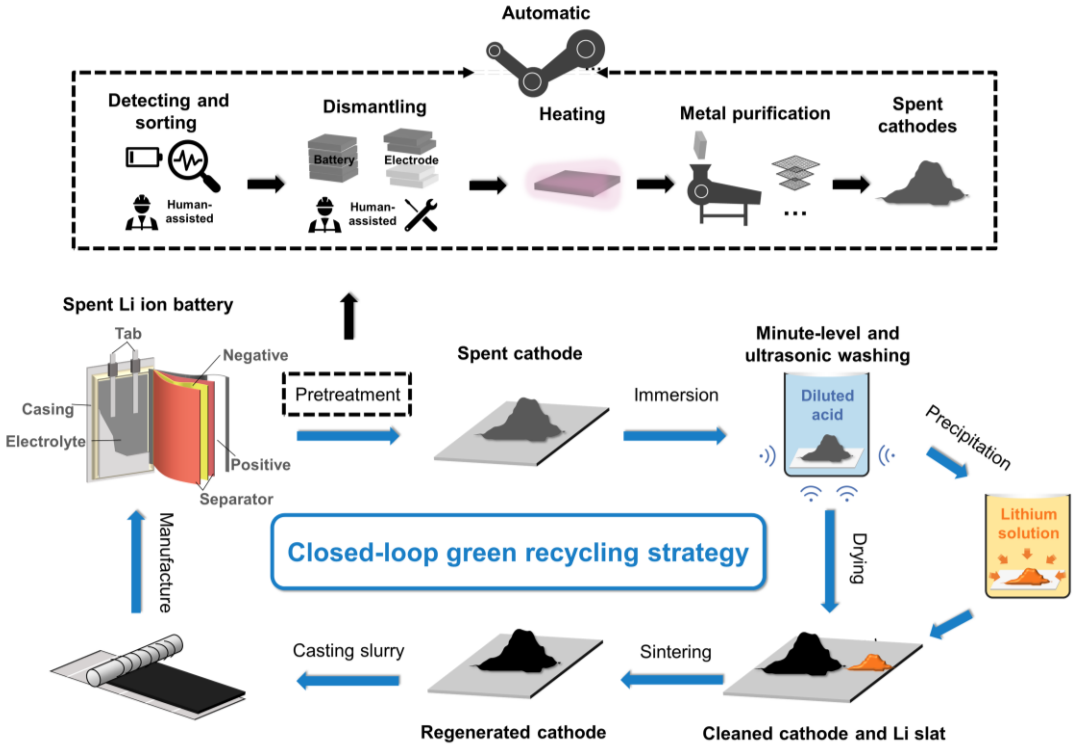

Fig. S1. Closed-loop green direct regeneration process with industrial-grade physical pretreatment, purification, and subsequent regeneration. The physical pretreatment includes sorting, discharging, dismantling, short-time heating, and multistage metal purification for collecting similar spent cathode and significantly diminishing metal foreign matter (e.g., Al, Cu). A similar pretreatment has been successfully implemented at a practical scale for material regeneration by companies such as Huayou New Energy Technology, GEM, Audi, Green Science Alliance, etc. [5-8] During the purification process, an optional precipitation step, employing either heating or a precipitant, is implemented to obtain lithium salts (such as Li_2CO_3 or LiOH) as a valuable lithium resource from residual pretreatment leachate containing lithium element.

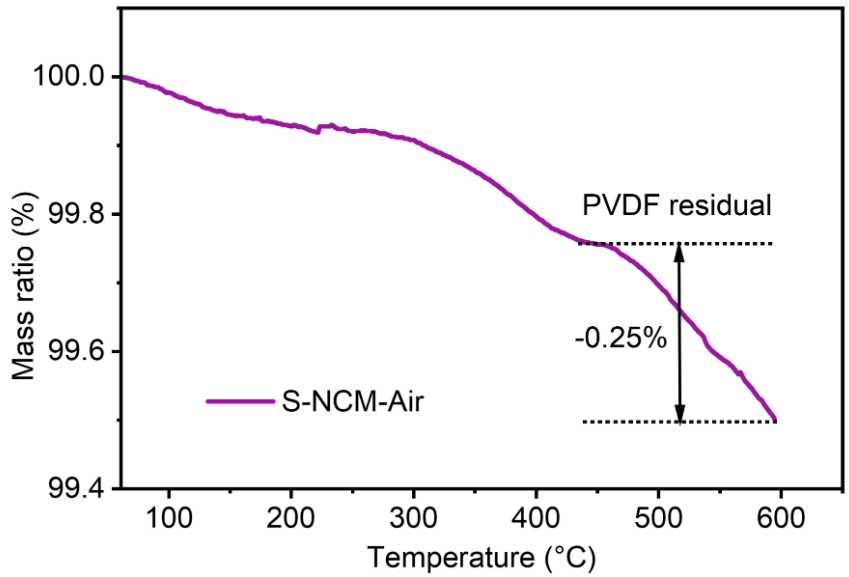

Fig. S2. The TGA curves of S-NCM at air atmosphere. Based on the heat behavior and mass loss of pure PVDF binder (**Fig. S24**), the S-NCM cathode exhibits a minimal mass loss of approximately 0.25% between 450°C and 600°C. This suggests that the residual PVDF binder within the S-NCM cathode is present in only trace amounts.

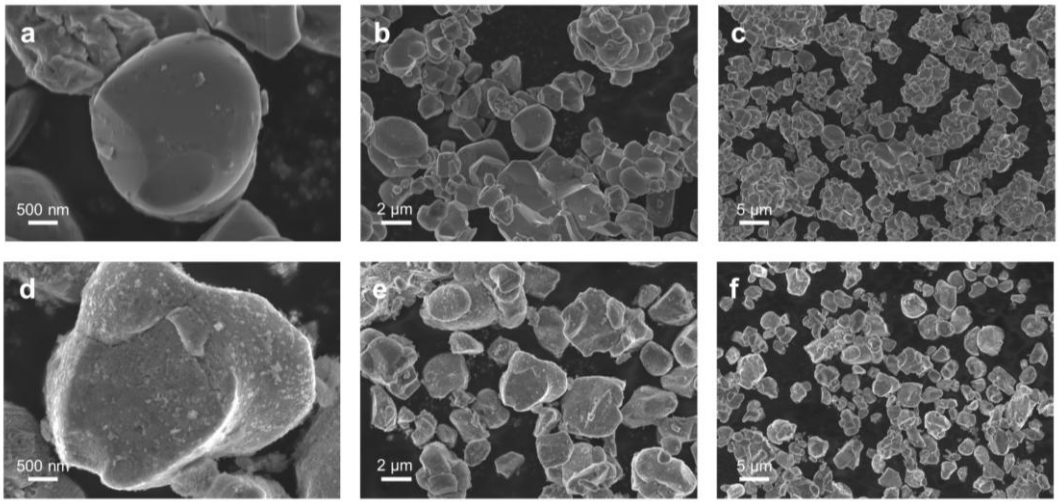

Fig. S3. SEM images of P-NCM and S-NCM cathodes. (a–c) the morphology of commercial P-NCM particles at different magnifications. (d–f) the morphology of S-NCM particles obtained from retired power batteries at different magnifications. The shape of a single particle remains unchanged even after prolonged cycling and physical pretreatment. Moreover, an uneven coating is observed on the surface of each particle, indicating the unique characteristics of these particles harvested from 250k-miles-serviced Li-ion batteries.

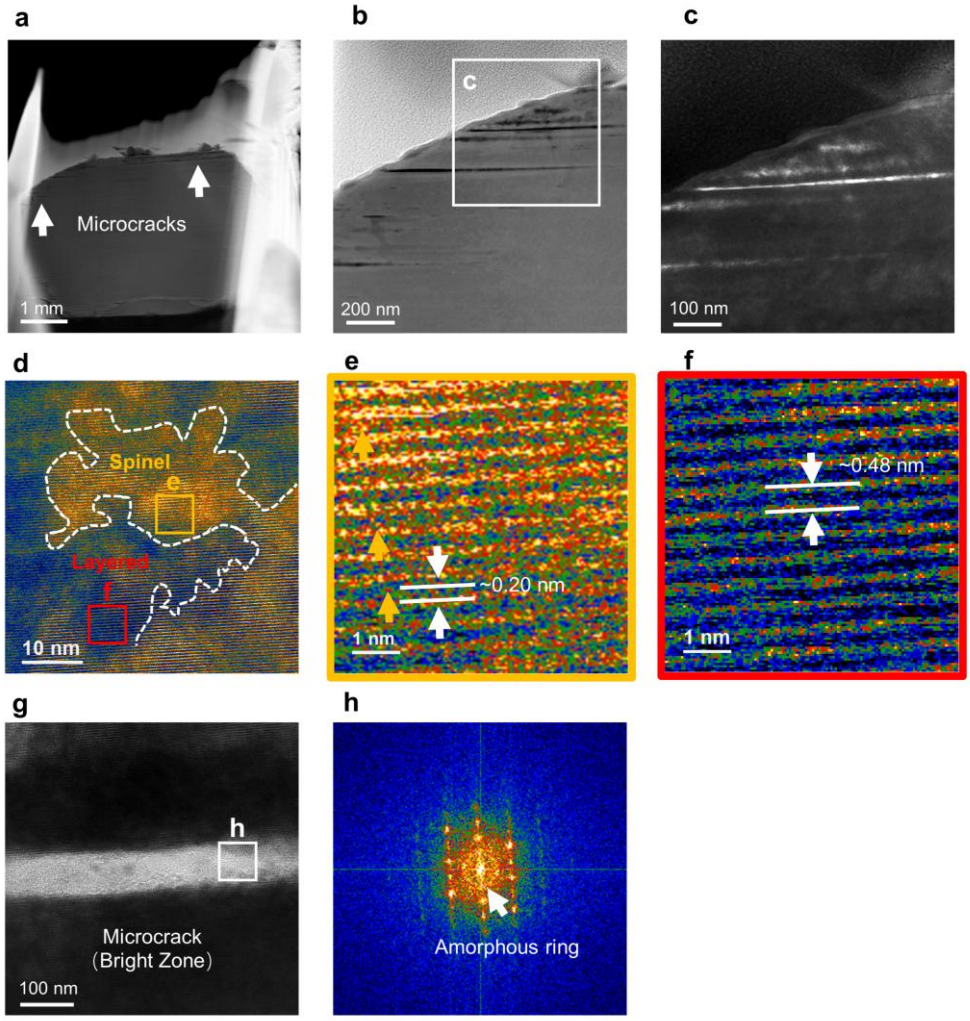

Fig. S4. Aberration-corrected STEM HAADF images of S-NCM particle from cross-section by FIB cutting. (a–b) The appearance (bright-field image) of the exposed cross-section for the S-NCM particle and (c) the dark-field image of an enlarged region. Some interior microcracks are visible and pointed out by a white arrow in cross-section, but the majority of them do not extend to the surface of the S-NCM particles. These cracks isolated from the electrolyte could lengthen the Li^+ transportation path during cycling tests. Bright lines observed in the dark-field image corresponded with the lattice dislocations and high strain. (d) The atomic arrangement near the cracks in the cross-section of S-NCM particles, and (e–f) an enlarged image of the selected area. Based on the observed space of (200) lattice plane is ~0.21 nm, the bright area represents the rock salt phase with a space group of Fm-3m and is different from a perfect layered structure (the enlarged dark area) that the representative (003) lattice plane spacing is ~0.48 nm. Yellow arrows indicate additional transition metal (TM) atoms located between the lithium layers. (g) A high-resolution atomic image of the bright region on behalf of the microcrack, and (h) the fast Fourier transform (FFT) pattern from the selected position is displayed. The broadened diffraction ring in the FFT pattern indicates the presence of amorphous impurities, likely originating from the penetration and decomposition of the electrolyte along cracks.

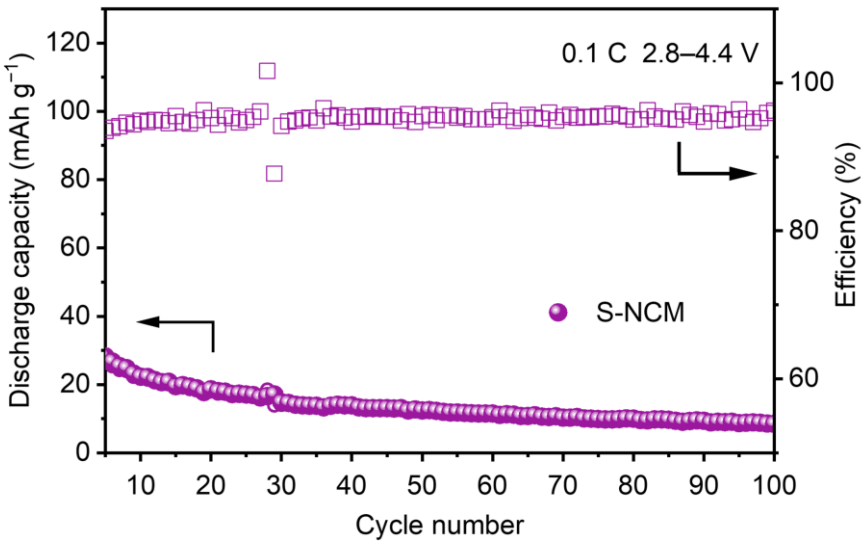

Fig. S5. The cycling performance of S-NCM material (1 C = 150 mAh g^{-1}).

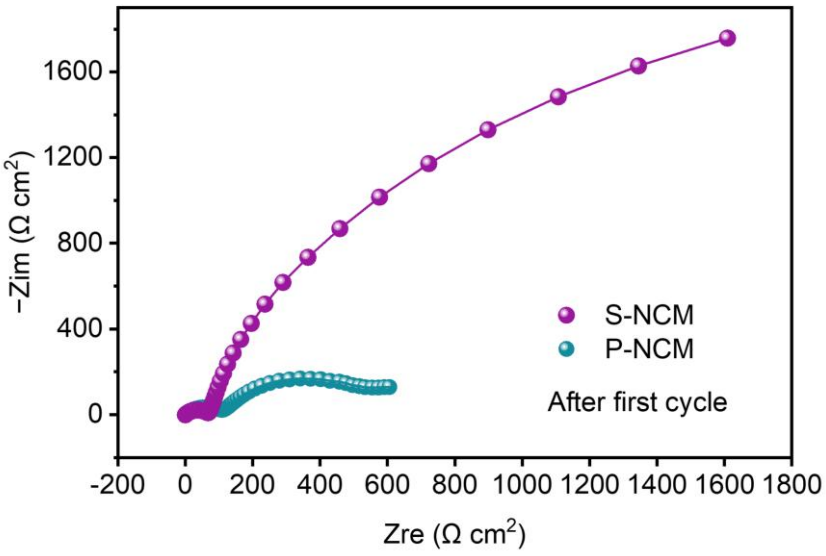

Fig. S6. Nyquist plots and fitting results (solid line) of S-NCM and P-NCM cathodes after first cycling from 0.01 Hz to 100 kHz. The equivalent circuit model for fitting is the same as the **Fig. 4f**.

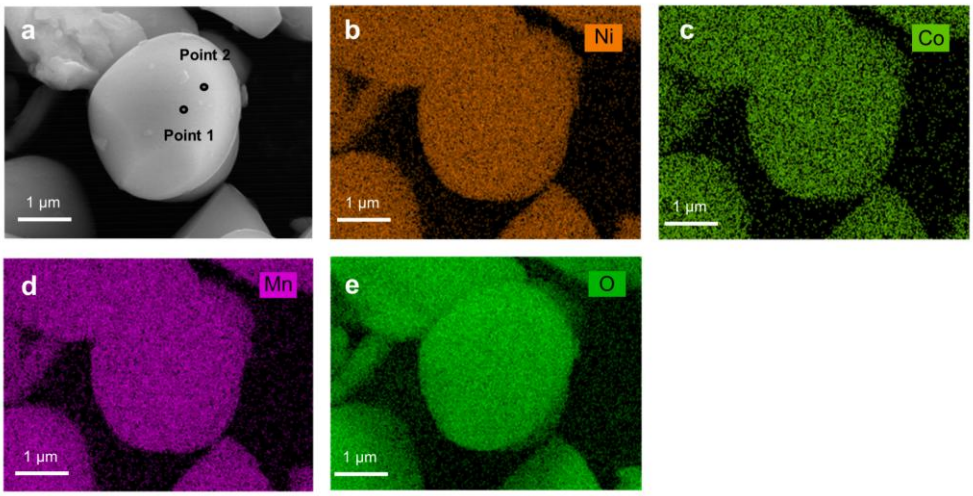

Fig. S7. SEM and EDS mapping images of P-NCM cathodes. (a) The microscopic morphology of P-NCM particles. Points 1 and 2 are scanned to determine the chemical composition by EDS analysis. The quantitative results of EDS spot analysis are listed in **Table S5**, keeping close with the transitional metal element ratio from ICP-OES analysis (**Table S4**). (b–e) Different element distributions of P-NCM particle.

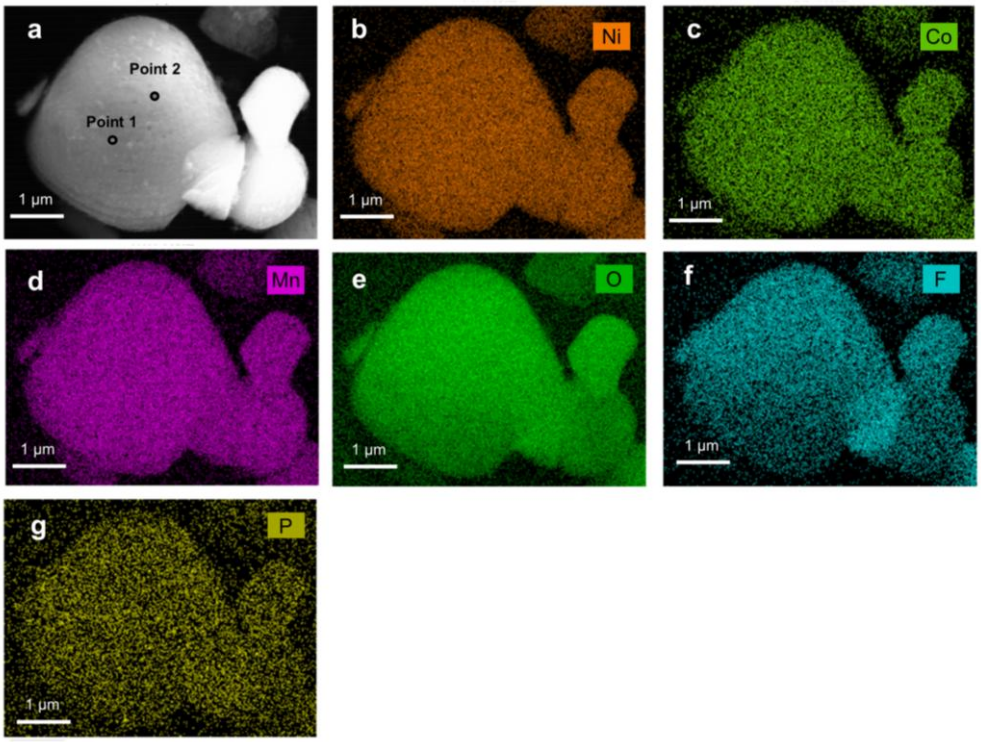

Fig. S8. SEM and EDS mapping images of S-NCM cathodes. (a) The microscopic morphology of S-NCM particles. Points 1 and 2 are scanned to precisely analyze impurity coating. The quantitative results of the EDS spot analysis are listed in **Table S6**. (b–g) The different element distribution of S-NCM particle. The surface of S-NCM has the substantial impurities containing F and P element impurities.

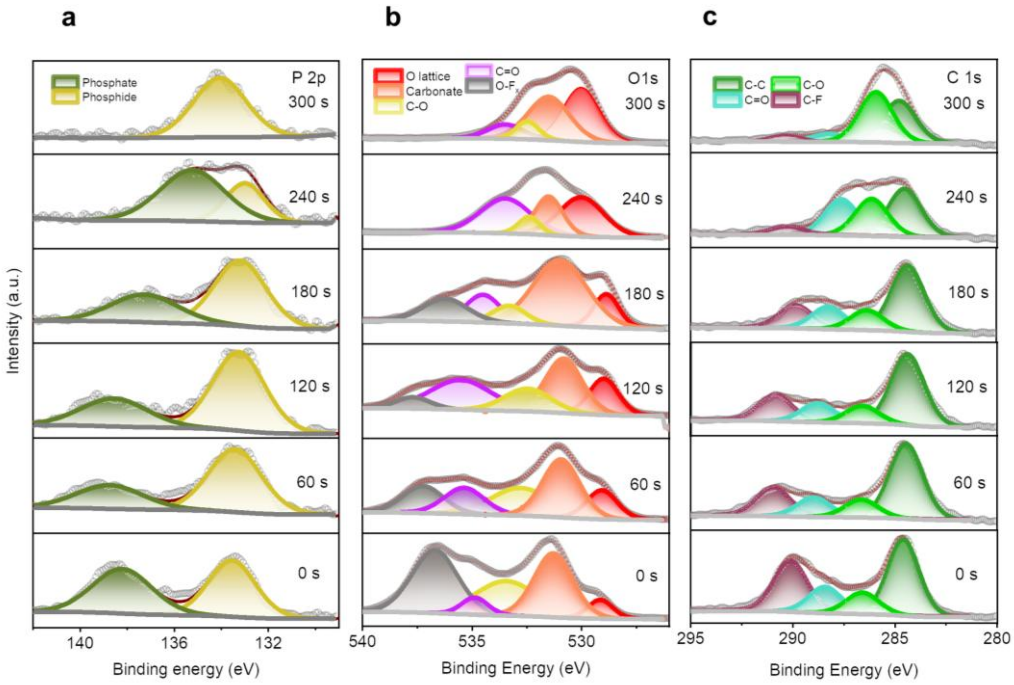

Fig. S9. Fitted peaks in the XPS fine spectras of S-NCM cathodes before and after etching 60 s, 120 s, 180 s, 240 s, and 300 s. The (a) P 2p XPS patterns. Similar to fluoride with gradient distribution, this residual phosphate and phosphide chemical state further support that the impurity residue on the surface of the S-NCM cathode primarily originates from the CEI layer and $LiPF_6$ or binder decomposition layer through calcination and mechanical pretreatment and without soaking in a poisonous organic solvent. The (b) O 1s and (c) C 1s XPS patterns exhibit similar characteristics to the F 1s XPS patterns and also show that the outer layer is mainly composed of organics containing C, O element, in contrast to the composition of the inner layer. This impurity layer has a similar composition to the CEI layer originating from electrolyte deposition. [9,10]

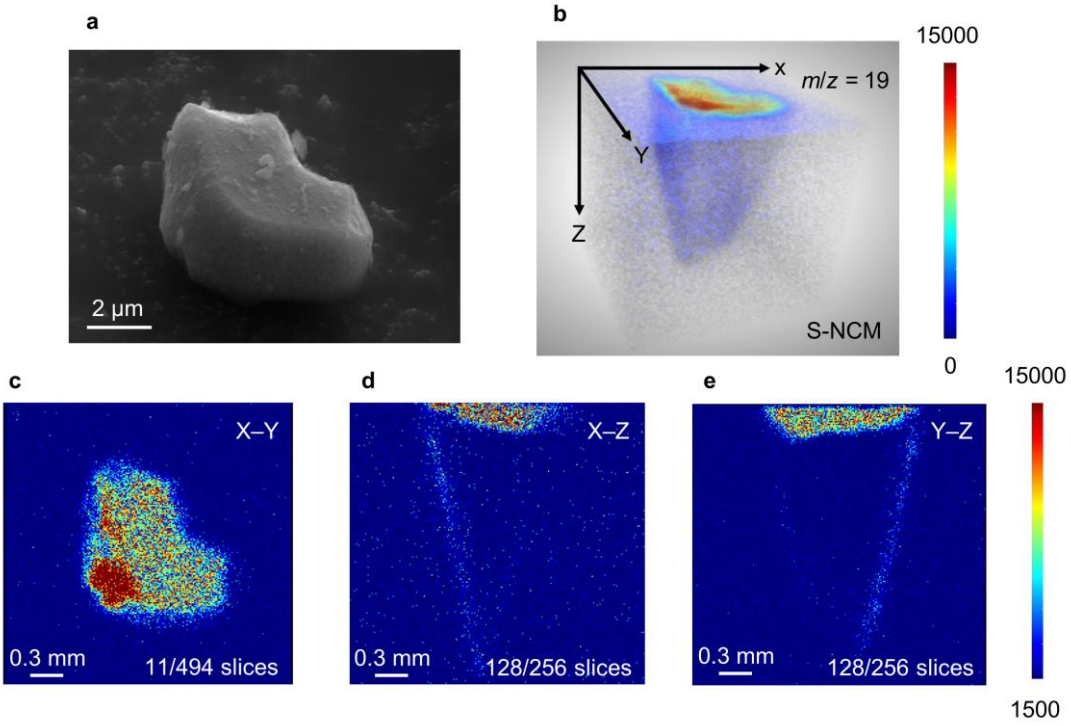

Fig. S10. SEM-ToF-SIMS characterization of selected S-NCM single particle. (a) SEM image and (b) corresponding pseudo-three-dimensional distribution of F^- segment (*m/z* = 19) in harvested S-NCM particle. Under ion beam bombardment, the single particles are stripped off layer by layer, and all vaporing ionic segments can be detected. Within the intensity bar, the red zone stands for higher relative concertation and the blue zone stands for lower concertation for select ionic segments. The representation direction of the following picture is based on the established spatial coordinate axis in this spatial figure. (c) X–Y, (d) X–Z, (e) Y–Z view of F element distribution map selected from a specific slice. The edge of the S-NCM particle exhibits a distinct accumulation of impurities. Through integrating different slices, **Videos S1**, **S2** provide visualizations of fluoride element distribution from the X–Y and X–Z views of the S-NCM cathodes.

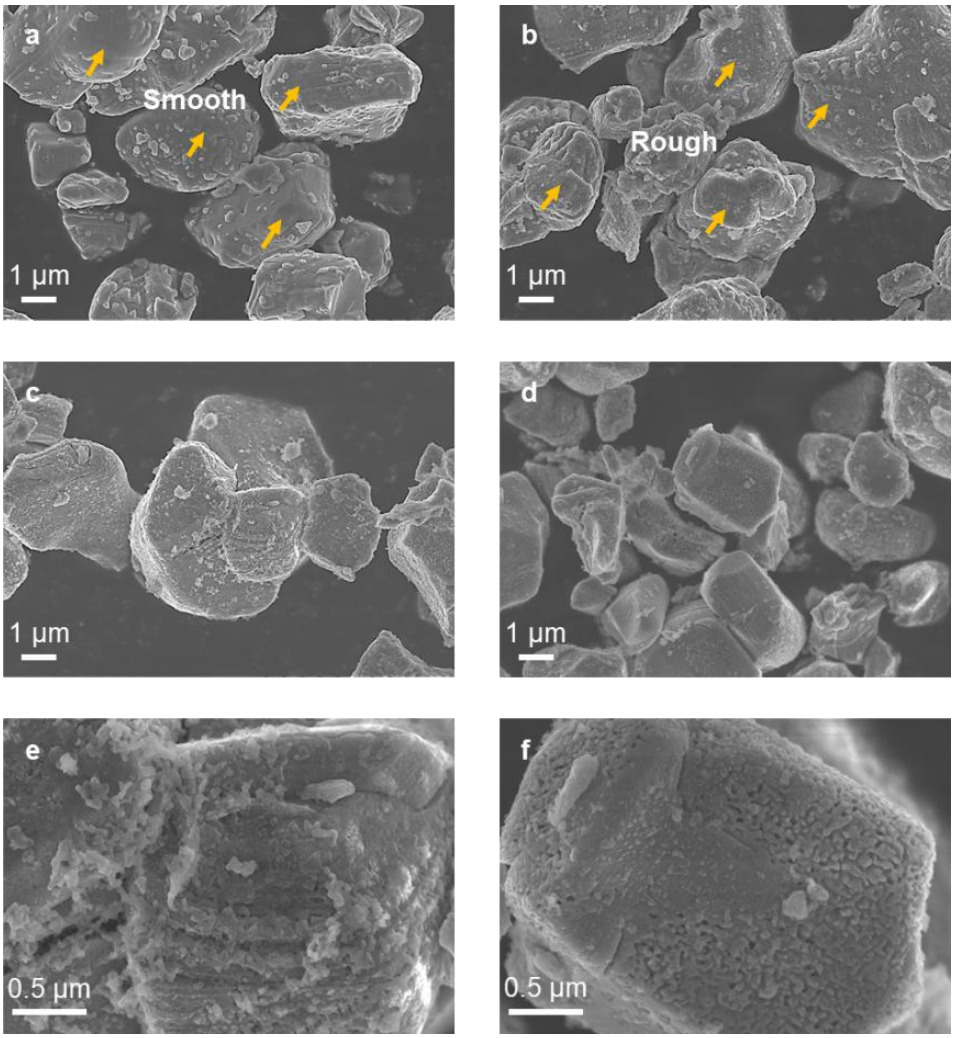

Fig. S11. The SEM images of four spent cathodes through mechanical and heating pretreatment illustrated in **Fig. S1**. (a) A sample; (b) B sample; (c, e) C sample; (d, f) D sample

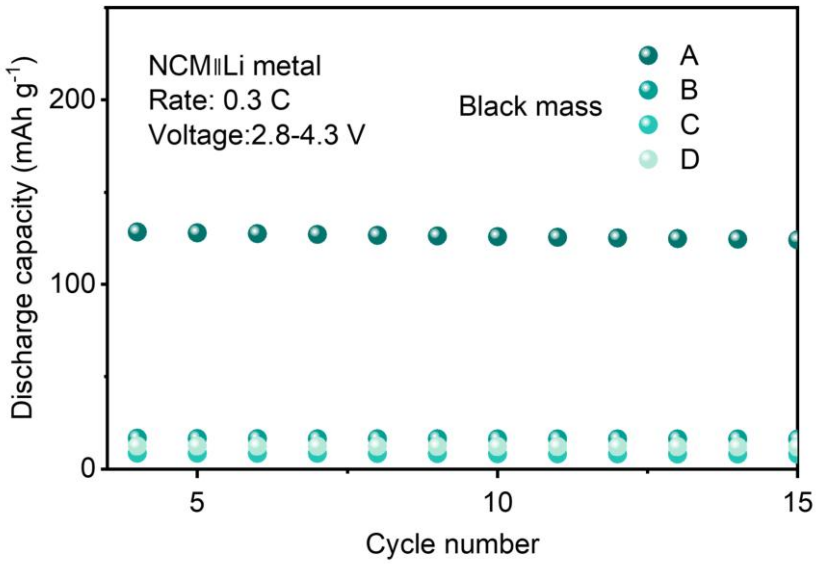

Fig. S12. The electrochemical performance of four spent cathodes

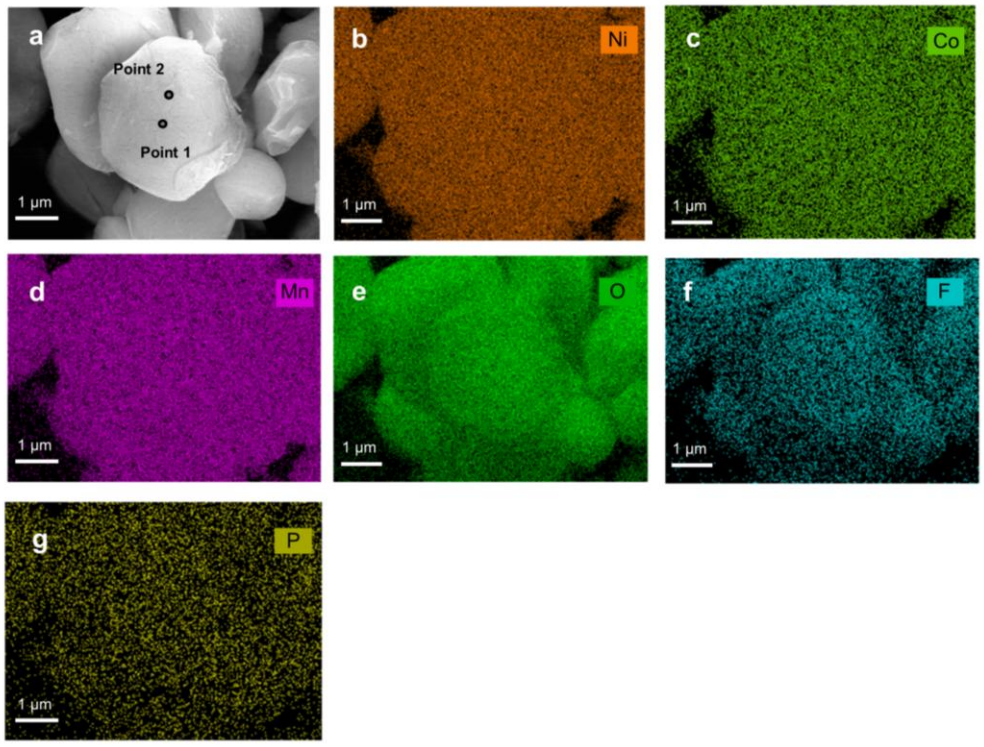

Fig. S13. SEM and EDS mapping images of C-NCM cathodes. (a) The microscopic morphology of C-NCM particles after soaking in 1 M HNO_3 solution. Within the magnified field of view, points 1 and 2 are scanned for precisely analyzing the evolution of residual impurities after cleaning. The quantitative results of point scanning are provided in **Table S8**. (b–g) The different element distribution of C-NCM particles after cleaning. The weakly acidic environment does not dissolve these transition metal oxide particles and allows them to retain their original morphology. It's noteworthy that some trace elements, such as F and P, may not be detected because of the EDS area analysis theory and the mapping results are susceptible to receiving interference from other signal peaks.

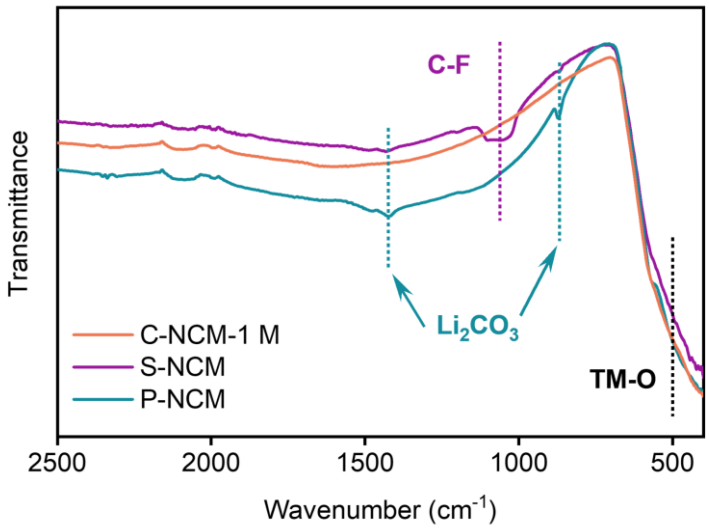

Fig. S14. FTIR spectrums of C-NCM-1 M, S-NCM, and P-NCM cathode powder. The absorption peaks in the wavenumber range of 400–600 cm^{-1} correspond to the bend vibration and asymmetric stretching of Ni–O, Co–O, and Mn–O bonds, and these peaks represented TM–O bonds (~500 cm^{-1}) in C-NCM-1 M cathodes have the same intensity as the P-NCM cathodes[11], which is supported that our proposed liquid-phase pretreatment is less destructive for the transition metal oxide matrix. Notably, the intensity of the TM–O peak for S-NCM cathodes is lower than the other sample due to the presence of an even impurity layer covering the surface.

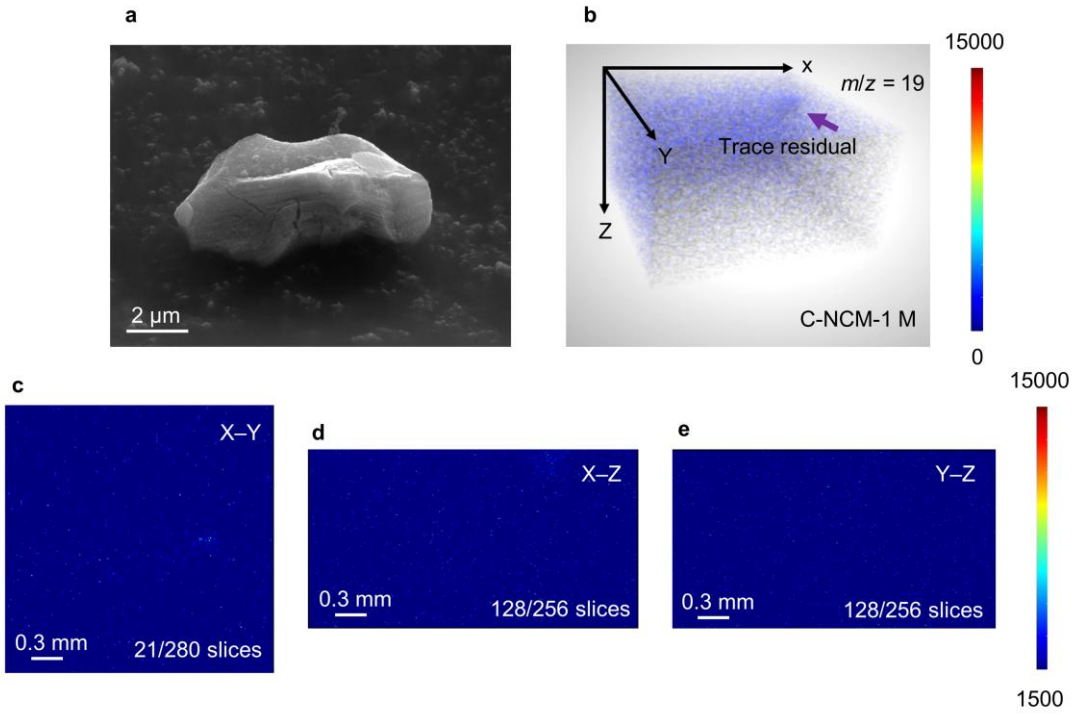

Fig. S15. SEM-ToF-SIMS characterization of selected C-NCM-1 M single particle. (a) SEM image and (b) corresponding pseudo-three-dimensional distribution of F element within C-NCM-1M particle. (c) X–Y, (d) X–Z, (e) Y–Z view of F element distribution map selected from a specific slice. The intensity bar range is the same as the mentioned bar. The imaging results support that nearly all impurities can be removed through appropriate treatment. However, the trace F element indicated by the purple arrow can still be observed in the spatial imaging. Based on all slices, **Videos S3, S4** provide dynamic visualizations of fluoride segment distribution in the X–Y and X–Z views of the C-NCM cathodes.

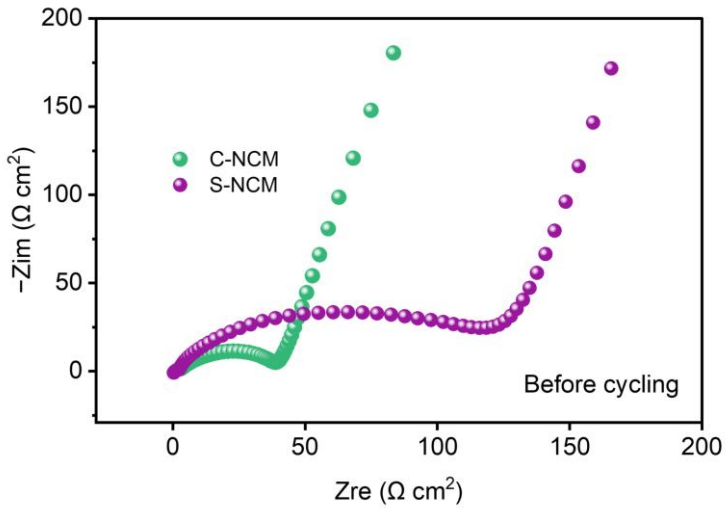

Fig. S16. The EIS measurement of C-NCM and S-NCM based on the assembled coin cell before cycling.

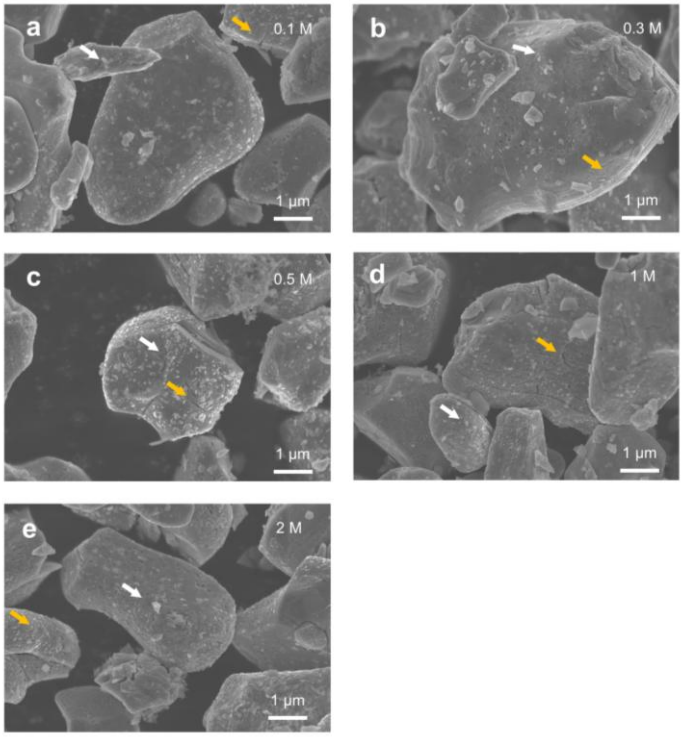

Fig. S17. SEM images of S-NCM cathodes soaking in different concentrations of HNO_3 solution for 5 minutes. All samples, even washing in high concentrations, show no obvious damage, and small clumps of residual material (indicated by the white arrow) may belong to lighter organic buried in the impurities layer. Currently, cracks (highlighted by yellow arrow) extending to the surface are exposed, which is beneficial to the contact between the degraded structure and the lithium source.

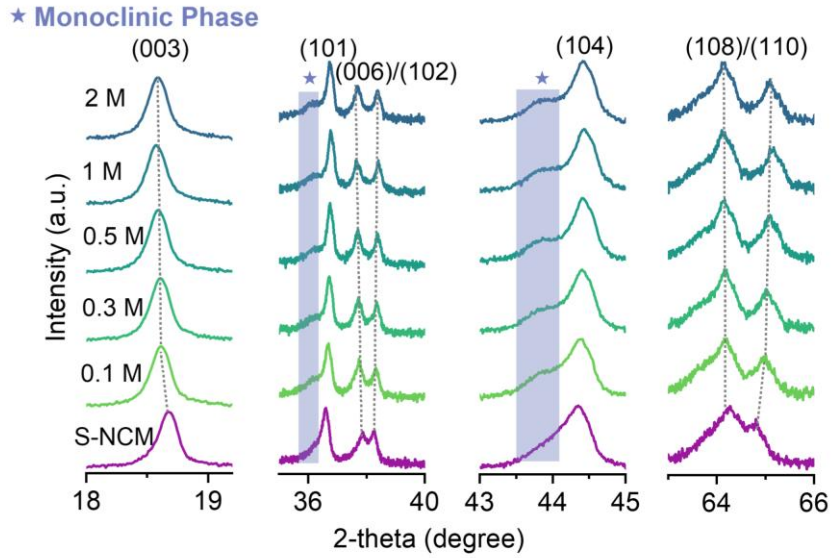

Fig. S18. The evolution of crystal structure within C-NCM cathodes obtained through cleaning in different concentrations of HNO_3 solution. The position of the (003) peak shifts to a lower angle, indicating that the pretreatment enlarges the crystal plane distance due to the extraction of Li^+ from the layered structure. Notably, the larger shift of (003) peak represented to layered structure does not occur in higher concentrations (> 0.1 M). However, a monoclinic phase caused by lithium extracting gradually grows from the matrix, and the splitting degree for the (006)/(102) and (108)/(110) peaks inconspicuous increases when the concentration exceeds 0.1 M. Consequently, the layered framework after acid cleaning has no collapse but some lattice distortion according to the lithium loss and the evident Jahn–Teller effect [12] during the pretreatment.

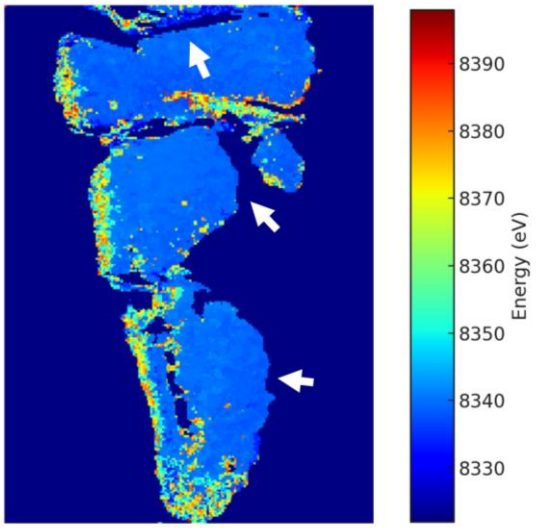

Fig. S19. The 2D TXM–XANES mappings of C-NCM-1M. A higher Ni oxidation state is present in the local surface area, indicating a degraded phase caused by Li extraction. However, more of the bulk area (indicated by white arrows) is exposed and retains a lower valence state, which can facilitate subsequent lithium replenishment along the layered structure without impurity barrier.

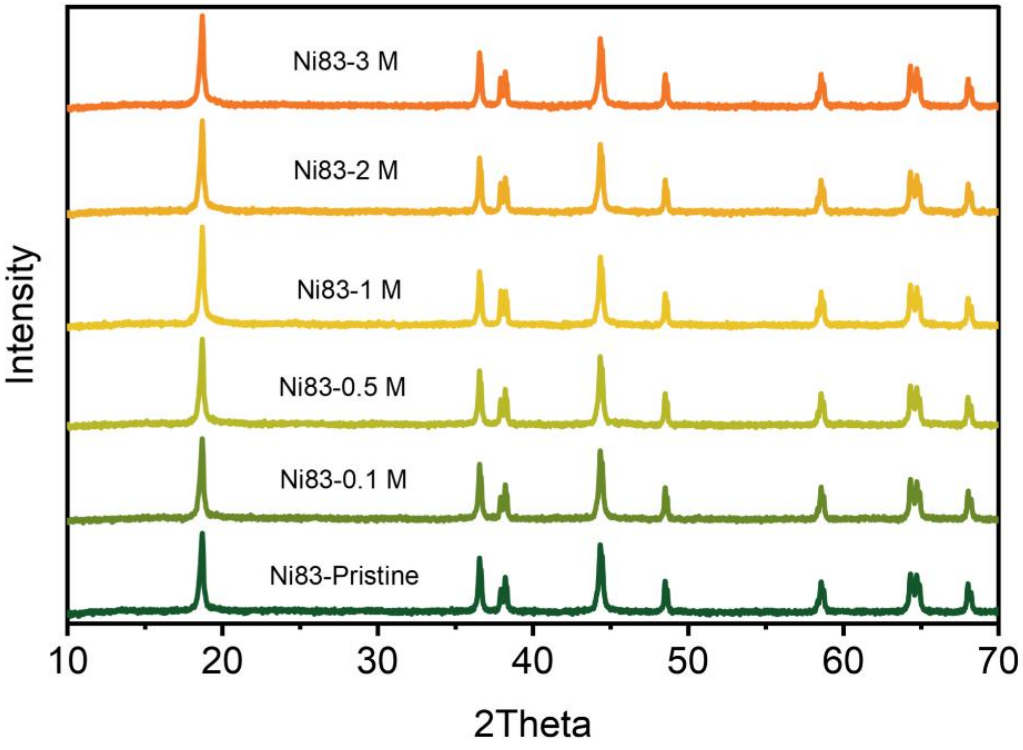

Fig. S20. The XRD pattern of Ni83 cathodes after soaking in acid with different concertation

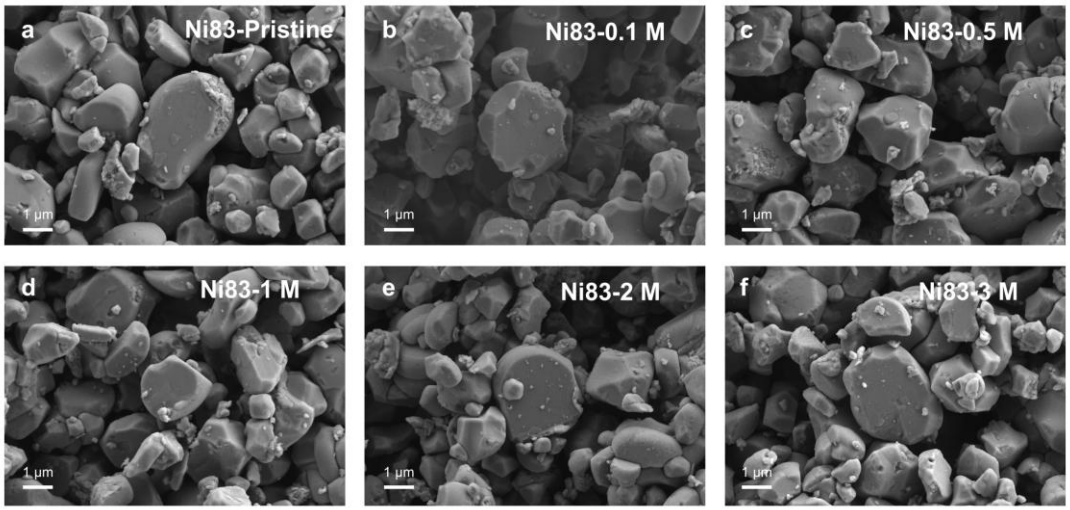

Fig. S21. SEM images of Ni83 cathodes after soaking in acid with different concertation

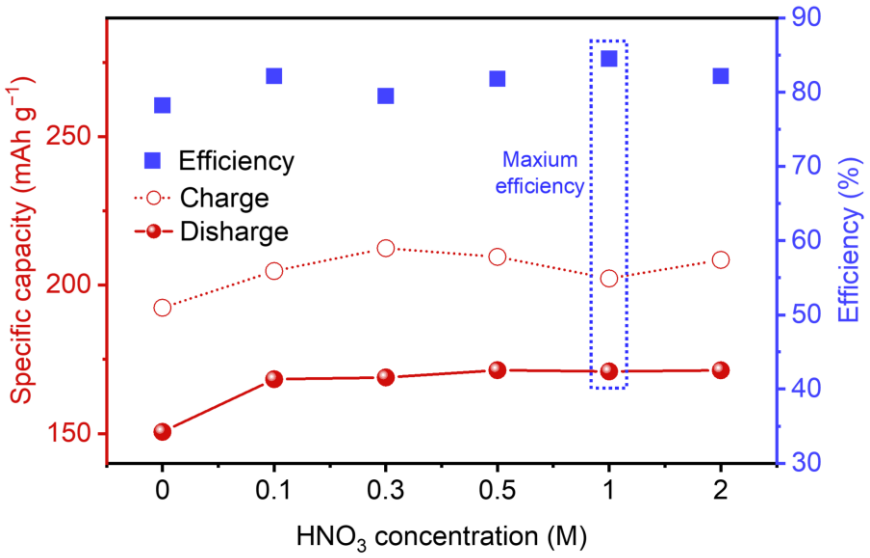

Fig. S22. 1st cycling performance of R-C-NCM regenerated from C-NCM cathode soaking in different concentration HNO_3 solution.

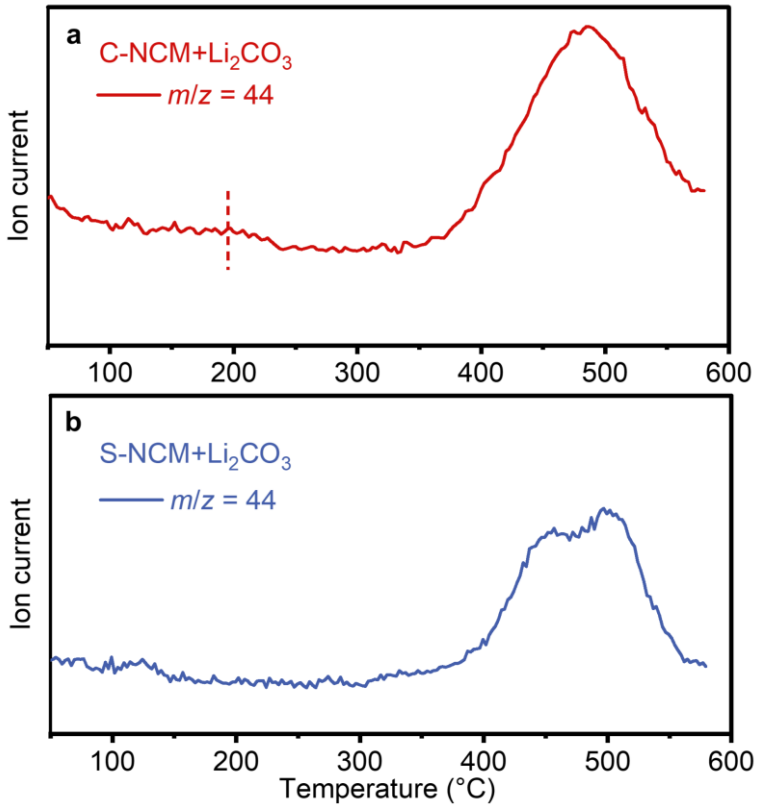

Fig. S23. MS results of two mixers with heating on oxygen atmosphere. (a) C-NCM cathodes and (b) S-NCM cathodes mixed with Li_2CO_3. Gas generation at around 200°C corresponds to the exothermic reactions exhibited in **Fig. 2f**. However, this temperature is far lower than the melting point of Li_2CO_3 (~420°C), indicating that lithium element in degraded NCM cathodes can be replenished at a unexpected low temperature. Moreover, the major gas production and lithium supplement show no significant change at higher temperature.

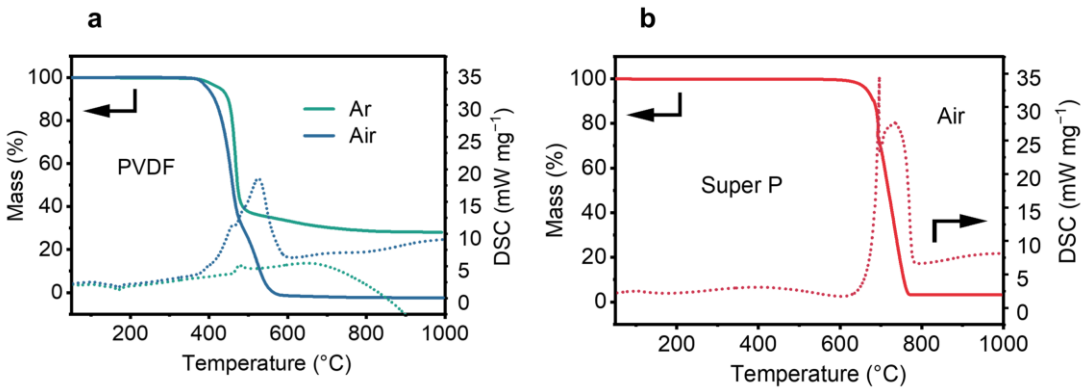

Fig. S24. The TG-DSC curves of binder (PVDF) and conductive carbon (Super P)

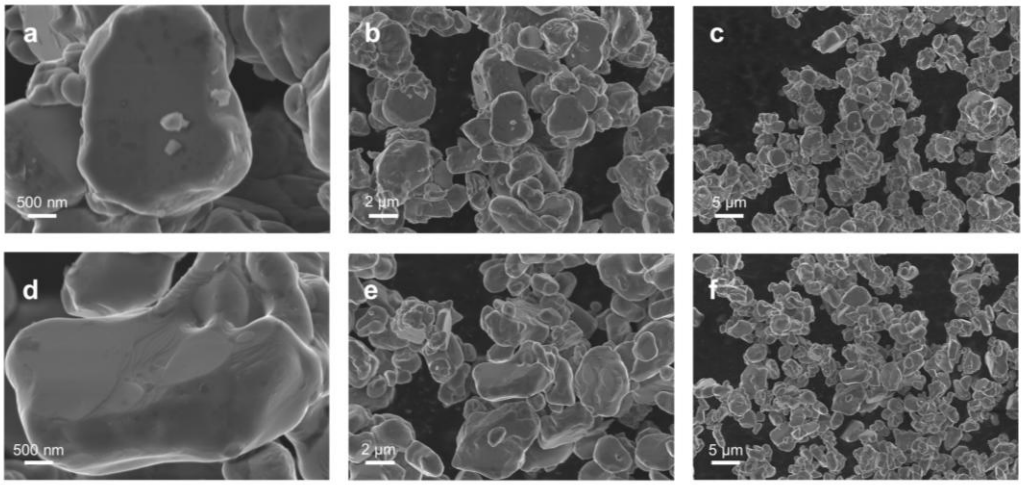

Fig. S25. SEM images of (a–c) R-S-NCM and (d–f) R-C-NCM cathode material.

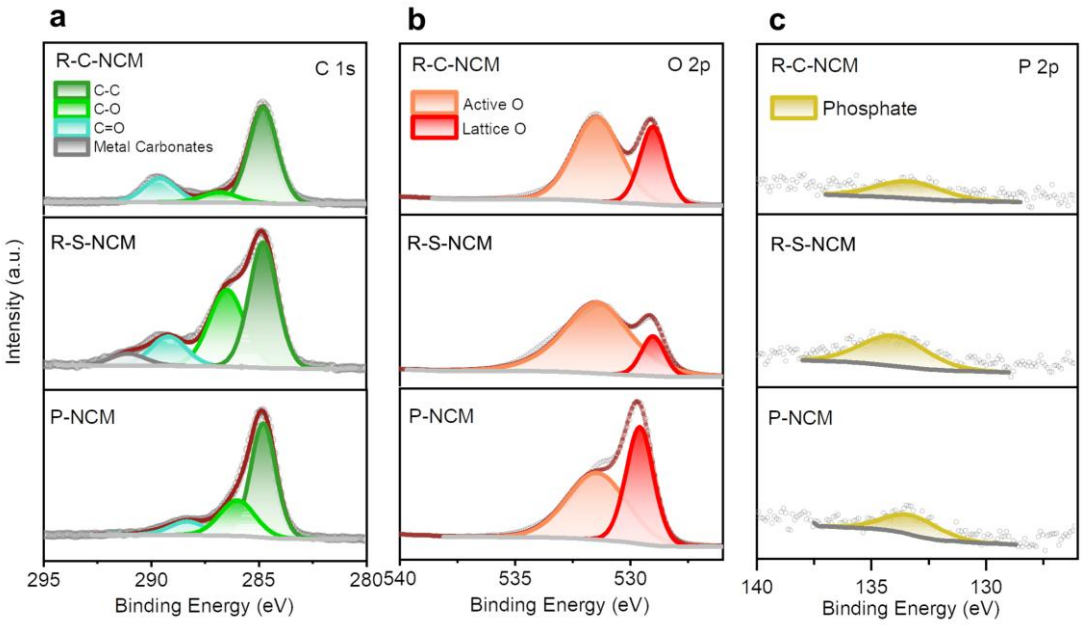

Fig. S26. The XPS fine spectra of R-C-NCM, R-S-NCM, and P-NCM cathode powders. (a) C 1s, (b) O 2p, (c) P 2p of XPS patterns. The surface of R-S-NCM cathodes has more residual alkali containing C and O elements when the cleaning pretreatment is not applied in direct regeneration. In addition to the F element, there are also some residues containing the P element, indicating the uncontrollable and complex transfer and reaction of impurities within R-S-NCM cathodes during direct regeneration. Hence, these residues and the interactions among different elements can significantly alter the surface properties. However, the XPS fine spectra of the P element for R-C-NCM and P-NCM are similar and has very weak peak, possibly identified to the signal disturbance.

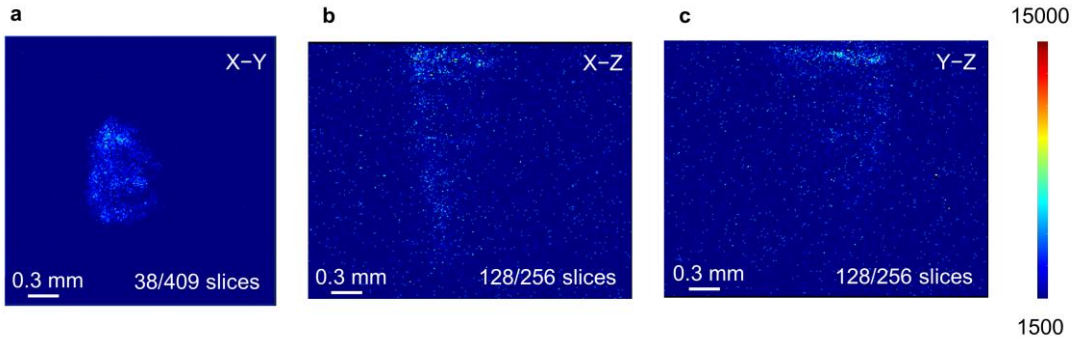

Fig. S27. SEM-ToF-SIMS characterization of selected R-S-NCM single particle.

(a) X–Y, (b) X–Z, (c) Y–Z view of F element distribution map selected from a specific slice. The impurities originally distributed on the surface of degraded cathodes are not entirely converted into escaped gas through long-term high-temperature exposure; instead, a portion of them penetrates the interior of the particles according to the considerable bright point located in the center area of above selected slices, compared with **Fig. S10**. These subtle changes are noteworthy, as they can impact the electrochemical properties of the material. **Videos S5**, **S6** provide dynamic visualizations of fluoride element distribution from the X–Y and X–Z views of the R-S-NCM cathodes, offering detailed insights into the distribution and evolution path of elements within the cathode material during the direct regeneration.

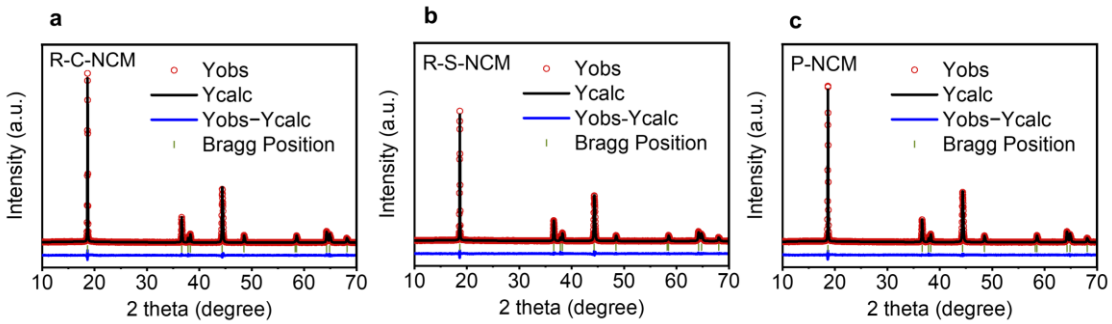

Fig. S28. The Rietveld refinement pattern between regenerated cathodes (R-C-NCM and R-S-NCM) and commercial P-NCM cathodes. Through refinement, the lattice parameter value can be compared in **Table S11**.

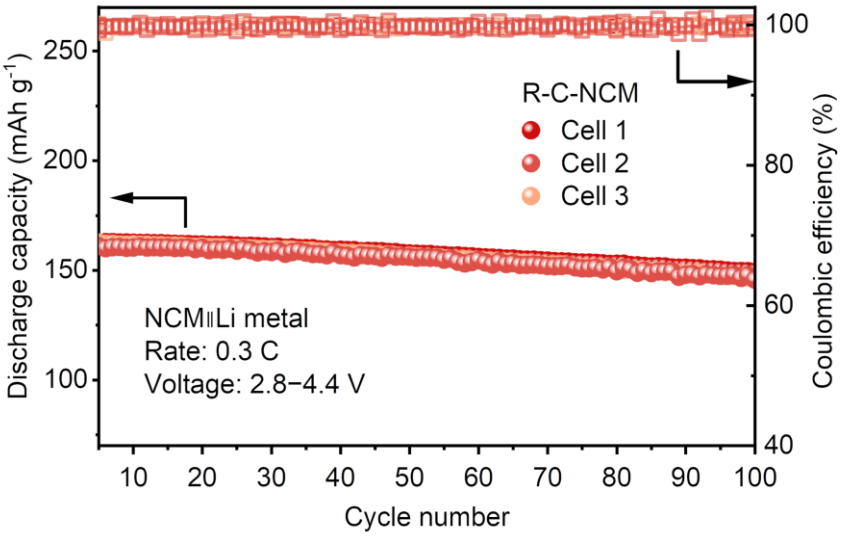

Fig. S29. The cycling performance of three coin-cells for R-C-NCM cathodes.

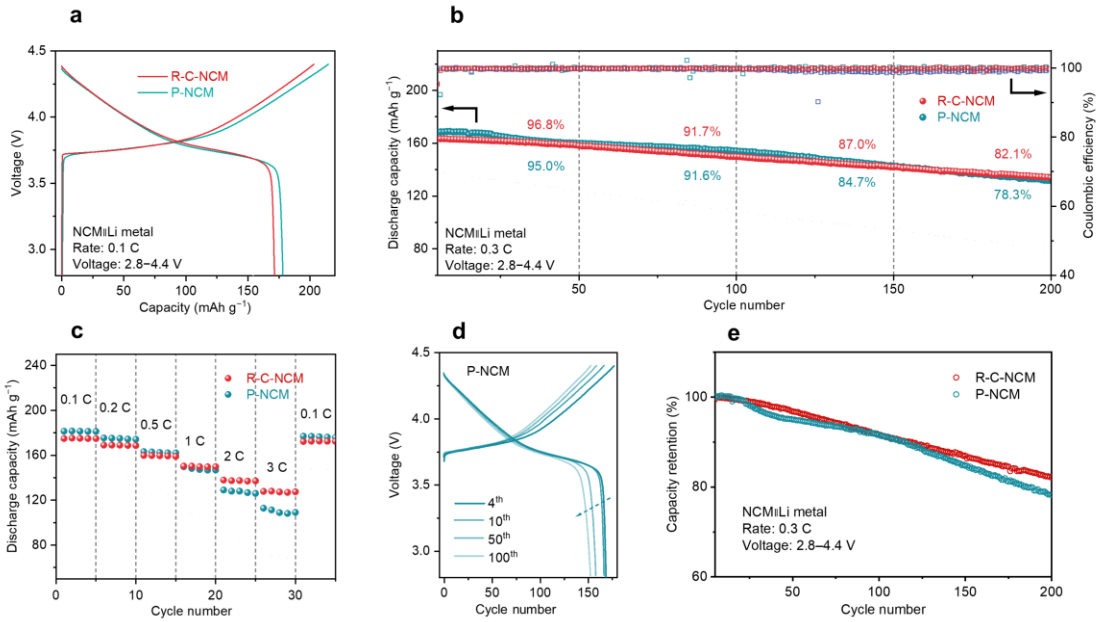

Fig. S30. Detailed comparation between R-C-NCM and P-NCM on the half cell.

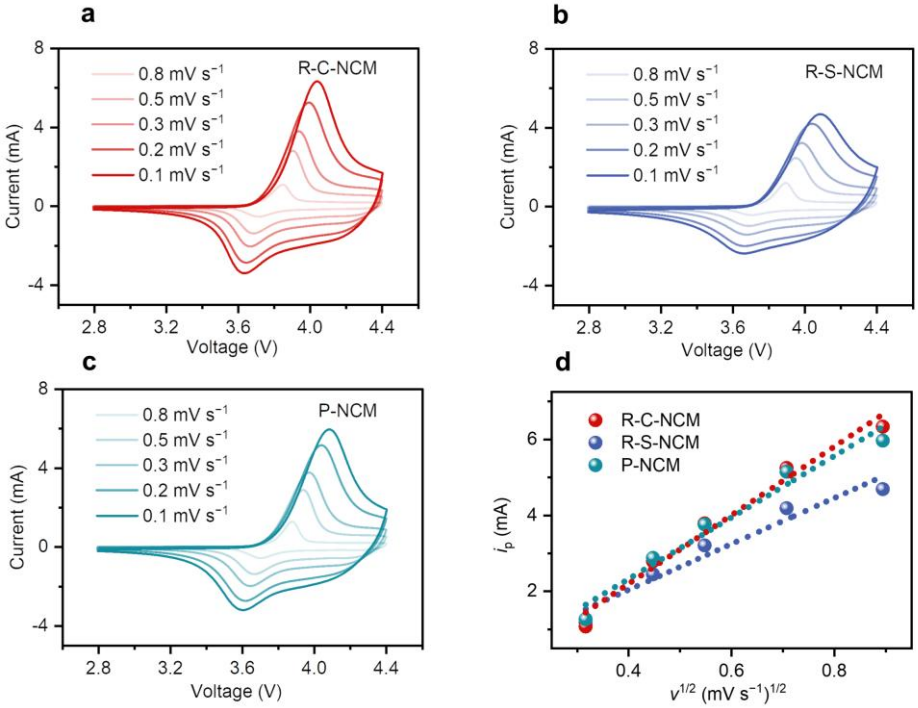

Fig. S31. CV curves at different scanning rates and fitting results of R-C-NCM, R-S-NCM, and P-NCM cathodes within a voltage range of 2.8–4.4 V. To determine the dynamic characteristics, the peak current (denoted as i_p) at every scanning speed is obtained. The fitting methods are shown in the 'Coin cell assembly and electrochemical performance' procedure (See **Materials and Methods** section). The area under the CV curve in the charge-discharge process decreases among the three samples when the current intensity increases. Because of excessive doping and severe surface polarization, the peak voltage of R-S-NCM is higher than that of R-C-NCM and P-NCM cathode particles. The difference is shown in the fitting linear, of which the slope is the lowest and can support the low Li^+ conductivity of R-S-NCM cathodes. Some details about all fitting curves can be seen in **Table S12**.

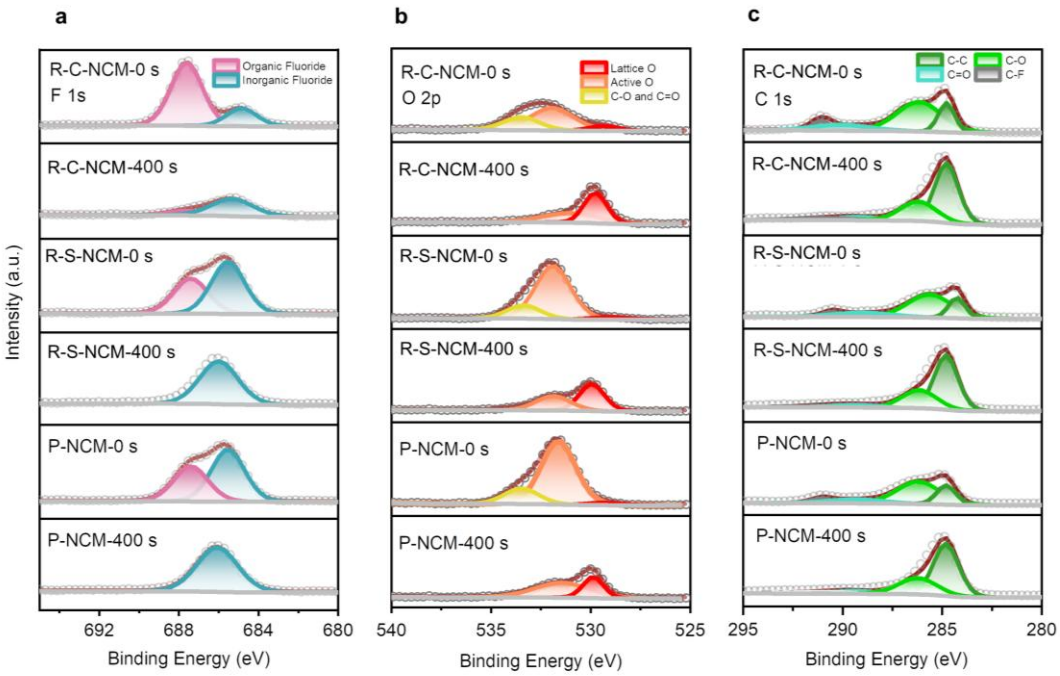

Fig. S32. The XPS fine spectra before and after etching 400 s from the CEI layer of R-C-NCM, R-S-NCM, and P-NCM cathode powders after 100 cycles.

(a) F 1s, (b) O 2p, (c) C 1s of XPS patterns. A comparison between R-C-NCM, R-S-NCM, and P-NCM cathodes reveals that the more organic fluoride and lattice oxygen are observed in R-C-NCM cathodes after 100 cycles within the voltage range of 2.8–4.4 V (0.3 C, 1 C = 150 mAh g^{-1}). By removing impurities, the R-C-NCM features a thinner CEI layer that contains reduced inorganic fluoride, which in turn suppresses interface impedance and enhances cycling stability.

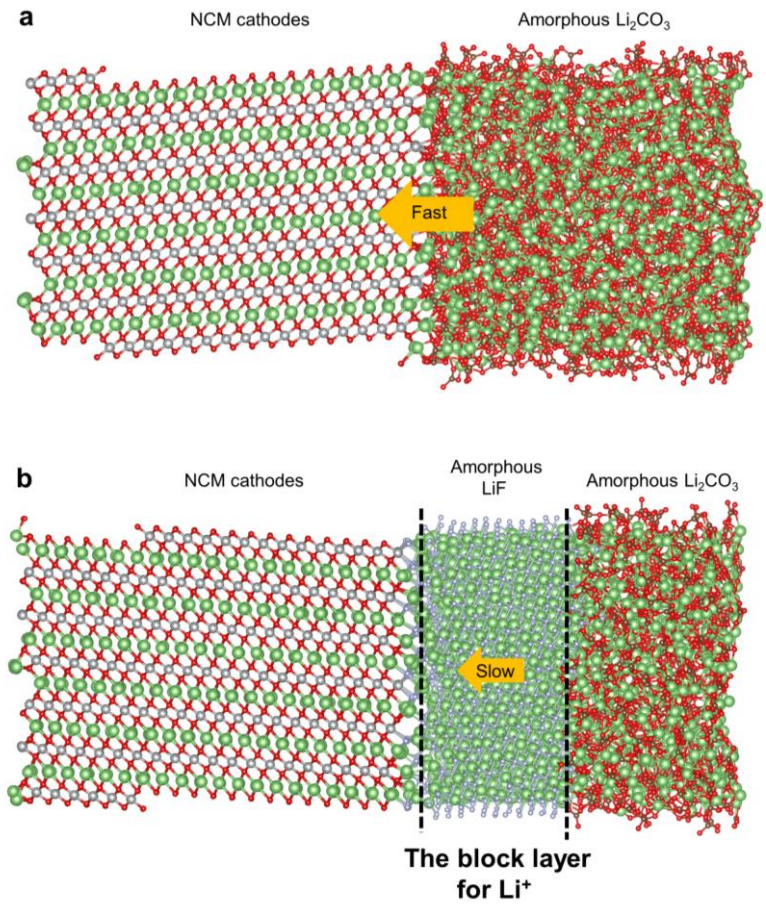

Fig. S33. The result of two molecular dynamics models after 20 ns based on the DFT simulation. These shape symbols are referred to the **Fig. 5a**. (a) NCM cathodes // Amorphous Li_2CO_3 // Amorphous Li_2CO_3 (lithium source). (b) NCM cathodes // Amorphous LiF // Amorphous Li_2CO_3 (lithium source).

Table S1. Reported pretreatment methods targeted to remove impurities from spent cathodes.

Pretreatment method	Input materials	Reported impurities in black mass	References
Transient heating	Anode electrode roll	Few metal impurities and organic	***Energy Environ. Sci***., 2023, 16, 6, 2561–2571
High powered ultrasound	Anode electrode roll	/	***Green Chem.***, 2021, 23, 13, 4710–4715
Ultrasonic cleaning	Cathode electrode roll	Al: 0.08 wt.%、Cu, Fe ＜0.01 wt.%	***Waste Manage.***, 2015, 46, 523–528
Calcination and sieving based on air jet	Cathode electrode pieces	Al: 0.1 wt.%	***J. Clean Prod.***, 2015, 108, 301–311
Pulsed discharge, water washing and sieving	Cathode electrode pieces	Al: 2.95 wt.%	***Waste Manage.***, 2021,125, 58–66
Cutting, magnet separation, attrition scrubbing and wet sieving	LIBs cell	Al: 0.8 wt.%, Cu: 1 wt.%	***J. Clean Prod.***, 2020, 260, 120869
Cutting, first-Sieving, magnet separation, calcination and sieving	LIBs cell	Al: 1.6 wt.%, Cu: 0.8 wt.%	***Sustain. Mater. Technol.***, 2020, 23, e00134
Pyrolysis	Electrode pieces	XPS analysis: F element on cathode (6.54 wt.%) and on anode (1.91 wt.%)	***J. Clean Prod.***, 2018, 199, 62–68
Pyrolysis on N_2 and CO_2 atmosphere	Electrode pieces	EDS analysis: F content in the cathodes was significantly reduced	***Waste Manage.***, 2023, 169, 342–350
Electromagnetic separation	Electrode pieces	High-purity of recovered electrode materials and Al foils (99.6% and 99.2%)	***Waste Manage.***, 2023, 166, 70–77

Table S2. Reported method of lab-simulated degraded cathodes before direct regeneration.

Input materials	Collecting spent cathodes method	References
Cell phone battery	Manually disassembly → **Cathode electrode soaking in NMP** → Heating in air	***Nat. Sustain.***, 2023, 6, 797-805
Pouch cells of spent LIBs	Discharging and drying → Manually separation→ **Cathode electrode soaking in DMC and NMP** → Suspension and water cleaning → Precipitate drying	***J. Am. Chem. Soc.***, 2022, 144, 44, 20306–20314
Spent batteries	Discharging and drying → Manually separation components→ **Cathode electrode rinsed with DMC**→ Solvothermal → Thermally treatment	***Adv. Mater.***, 2023, 2307091
Commercial LFP cells through 6,500 cycles	Manually disassembly → **Cathode electrode soaking in DMC and NMP** → Suspension and separation → Precipitate drying	***Joule***, 4, 12, 2609–2626
Pouch-type batteries from the battery packs of retired EVs	Manually cutting open and separation → **Cathode electrode rinsed with DMC** → Thermally treatment → Vibrational sieving	***Cell Rep. Phys. Sci.***, 3, 100741

Table S3. Metal scraps analysis of S-NCM collected from industrial-level pretreatment.

Size Range/ um	Total	5≤X≤ 15	15≤X≤ 25	25≤X≤ 50	50≤X≤ 100	150≤X≤ 200	200≤X≤ 400	400≤X≤ 600	600≤X≤ 1000	1000 ≤X
NCM	35	35	0	0	0	0	0	0	0	0
Fe-Cr	1	1	0	1	0	0	0	0	0	0
Zr alloy	2	0	0	0	0	0	0	0	0	0
Miscella neous	2	2	0	0	0	0	0	0	0	0
Sn	0	0	0	0	0	0	0	0	0	0
Zn alloy	0	0	0	0	0	0	0	0	0	0
Zn-O	0	0	0	0	0	0	0	0	0	0
Cu (Zn)	0	0	0	0	0	0	0	0	0	0
Al alloy	0	0	0	0	0	0	0	0	0	0
Cu alloy	0	0	0	0	0	0	0	0	0	0

Table S4. Chemical composition of the sample based on the result of ICP-OES.

Sample	Chemical composition
R-C-NCM	$Li_{1.02}Ni_{0.55}Mn_{0.30}Co_{0.15}O_2$
R-S-NCM	$Li_{1.04}Ni_{0.55}Mn_{0.30}Co_{0.15}O_2$
P-NCM	$Li_{0.99}Ni_{0.55}Mn_{0.30}Co_{0.15}O_2$
S-NCM	$Li_{0.86}Ni_{0.55}Mn_{0.30}Co_{0.15}O_2$
C-NCM	$Li_{0.62}Ni_{0.55}Mn_{0.30}Co_{0.15}O_2$

Table S5. Chemical composition of selected points on the surface of P-NCM cathodes by EDS spot analysis.

Element	The ratio of elements for Point 1 /wt.%	The ratio of elements for Point 2 /wt.%
C	11.44	15.52
O	36.96	40.48
F	1.17	1.37
Al	0.39	0.39
P	0.00	0.00
Mn	14.16	11.83
Co	8.00	6.65
Ni	27.88	23.76

Table S6. Chemical composition of selected points on the surface of S-NCM cathodes by EDS spot analysis.

Element	The ratio of elements for Point 1 /wt.%	The ratio of elements for Point 2 /wt.%
C	14.69	13.06
O	36.75	32.43
F	3.20	2.04
Al	0.23	0.17
P	0.13	0.20
Mn	12.38	14.07
Co	6.91	8.21
Ni	25.69	29.82

Table S7. More details about four spent cathodes.

Type	Industrial input	Chemical composition
A	Pristine cathode electrodes to be assembled batteries	$Li_{1.00}Ni_{0.58}Mn_{0.30}Co_{0.11}O_2$
B	EVs batteries after electrolyte filling and formation	$Li_{0.95}Ni_{0.58}Mn_{0.30}Co_{0.12}O_2$
C	EVs batteries having completed 125k miles of service	$Li_{0.94}Ni_{0.57}Mn_{0.29}Co_{0.15}O_2$
D	EVs batteries having completed 250k miles of service	$Li_{0.87}Ni_{0.57}Mn_{0.29}Co_{0.15}O_2$

Table S8. Chemical composition of selected points on the surface of C-NCM cathodes after soaking in 1 M HNO_3 solution by EDS spot analysis.

Element	The ratio of elements for Point 1 /wt.%	The ratio of elements for Point 2 /wt.%
C	11.54	12.96
O	30.00	31.47
F	0.00	1.23
Al	0.18	0.22
P	0.00	0.00
Mn	15.07	14.02
Co	9.37	8.83
Ni	33.84	31.26

Table S9. The dissolution of metal of 250 mL of washing acid filtrate. The collected filtrate is diluted with deionized water to 250 mL after cleaning 5 g of spent cathode powder with 50 mL of 1 M HNO_3 solution, following the 'Collecting and Cleaning Degraded Cathode Materials' procedure (See **Materials and Methods** section).

Element	Concentration/ppm
Li	572.7
Ni	803.1
Co	256.9
Mn	615.3

Table S10. The result of ICP-OES analysis for Ni83 cathodes after soaking in acid with different concertation.

Sample	Li/wt%	Ni/wt%	Co/wt%	Mn/wt%	Chemical composition
Ni83-Pristine	6.44	44.2	3.24	5.84	$Li_{1.01}Ni_{0.82}Co_{0.06}Mn_{0.12}O_2$
Ni83-0.1 M	6.54	46.6	3.35	6.17	$Li_{0.98}Ni_{0.82}Co_{0.06}Mn_{0.12}O_2$
Ni83-0.5 M	6.38	45.7	3.27	6.03	$Li_{0.97}Ni_{0.82}Co_{0.06}Mn_{0.12}O_2$
Ni83-1 M	6.45	46.3	3.29	6.11	$Li_{0.97}Ni_{0.83}Co_{0.06}Mn_{0.12}O_2$
Ni83-2 M	6.32	45.4	3.19	5.97	$Li_{0.97}Ni_{0.83}Co_{0.06}Mn_{0.12}O_2$
Ni83-3 M	6.76	49.0	3.43	6.43	$Li_{0.96}Ni_{0.83}Co_{0.06}Mn_{0.12}O_2$

Table S11. Rietveld refinement results of all samples.

Sample	The (003) peak position /°	The (104) peak position /°	$I_{(003)}/I_{(104)}$	a/Å	c/Å	c/a	V/Å^3	Ni^{2+} in Li layer/%	R_{wp}	χ^2
R-C-NCM	18.68	44.38	3.004	2.869	14.225	4.957	101.43	5.35%	2.948	6.090
R-S-NCM	18.66	44.32	2.697	2.874	14.240	4.954	101.883	6.37%	3.170	6.690
P-NCM	18.68	44.38	2.946	2.872	14.233	4.957	101.638	5.80%	3.037	6.490

Table S12. The slope and R-square of the fitting lines from the CV curves at different scan rates.

	R-C-NCM	R-S-NCM	P-NCM
Slope	9.03016 ± 0.82300	6.04587 ± 0.82462	8.09791 ± 0.88569
R-Square	0.97569	0.94714	0.96536

3. Supplementary Videos

Video S1. The fluoride element distribution from the X–Y views of the S-NCM cathodes
Video S2. The fluoride element distribution from the X–Z views of the S-NCM cathodes
Video S3. The fluoride element distribution from the X–Y views of the C-NCM cathodes
Video S4. The fluoride element distribution from the X–Z views of the C-NCM cathodes
Video S5. The fluoride element distribution from the X–Y views of the R-S-NCM cathodes
Video S6. The fluoride element distribution from the X–Z views of the R-S-NCM cathodes

Supplemental References

1. Elgrishi, N. *et al*.. A practical beginner's guide to cyclic voltammetry. (2018). *J. Chem. Educ*. **95**, 197–206.
2. Shaju, K. M., Subba Rao, G. V., & Chowdari, B. V. R. Influence of Li-ion kinetics in the cathodic performance of layered $Li(Ni_{1/3}Co_{1/3}Mn_{1/3})O_2$. (2004). *J. Electrochem. Soc* **151**, A1324.
3. Perdew, J. P., Burke, K., & Ernzerhof, M. (1996). Generalized gradient approximation made simple. *Phys. Rev. Lett.* **77**, 3865–3868.
4. Akkermans, R. L. C., Spenley, N. A., & Robertson, S. H. COMPASS III: automated fitting workflows and extension to ionic liquids. (2021). *Mol. Simul.* **47**, 540–551.
5. Recycling Industry (2023).https://www.huayou.com/en/products/recycling-industry.
6. Power Battery Recycling Business (2023). https://en.gem.com.cn/Products/info.aspx?itemid=5841.
7. Wegener, K., Andrew, S., Raatz, A., Dröder, K., & Herrmann, C. (2014). Disassembly of electric vehicle batteries using the example of the Audi Q5 hybrid system. Procedia CIRP 23, 155–160.
8. PR-newswire (2023). Green Science Alliance Made Lithium Ion Battery Cathode Directly from Recycle Material Named "Black Mass". https://www.prnewswire.com/news-releases/green-science-alliance-made-lithium-ion-battery-cathode-directly-from-recycle-material-named-black-mass-301905799.html
9. Li, W., Dolocan, A., Oh, P., Celio, H., Park, S., Cho, J., & Manthiram, A. (2017). Dynamic behaviour of interphases and its implication on high-energy-density cathode materials in lithium-ion batteries. *Nat. Commun.* **8**, 14589.
10. Zhou, Y., Su, M., Yu, X., Zhang, Y., Wang, J. G., Ren, X., Cao, R., Xu, W., Baer, D. R., Du, Y., *et al.* (2020). Real-time mass spectrometric characterization of the solid–electrolyte interphase of a lithium-ion battery. *Nat. Nanotechnol.* **15**, 224–230.
11. Zhou, H., Zhao, X., Yin, C., & Li, J. (2018). Regeneration of $LiNi_{0.5}Co_{0.2}Mn_{0.3}O_2$ cathode material from spent lithium-ion batteries. *Electrochim. Acta* **291**, 142–150.
12. Arroyo y de Dompablo, M. E., Van der Ven, A., & Ceder, G. (2002). First-principles calculations of lithium ordering and phase stability on Li_xNiO_2. *Phys. Rev. B - Condens*. Matter Mater. Phys. **66**, 1–9.